



Quantitative nanoscale tracking of oxygen vacancy diffusion inside single ceria grains by *in situ* transmission electron microscopy

Yong Ding^{1,*†}, YongMan Choi^{2,†}, Yu Chen¹, Ken C. Pradel¹, Meilin Liu^{1,*}, Zhong Lin Wang^{1,3,*}

¹ School of Materials Science and Engineering, Georgia Institute of Technology, Atlanta, GA 30332-0245, United States

² College of Photonics, National Chiao Tung University, Tainan 71150, Taiwan

³ Beijing Institute of Nanoenergy and Nanosystems, Chinese Academy of Sciences, Beijing 100083, PR China

Oxygen vacancy formation and migration in ceria is critical to its electrochemical and catalytic properties in systems for chemical and energy transformation, but its quantification is rather challenging especially at atomic-scale because of disordered distribution. Here we report a rational approach to track oxygen vacancy diffusion in single grains of pure and Sm-doped ceria at $-20\text{ }^{\circ}\text{C}$ to $160\text{ }^{\circ}\text{C}$ using *in situ* (scanning) transmission electron microscopy ((S)TEM). To create a gradient in oxygen vacancy concentration, a small region ($\sim 30\text{ nm}$ in diameter) inside a ceria grain is reduced to the C-type $\text{CeO}_{1.68}$ phase by the ionization or radiolysis effect of a high-energy electron beam. The evolution in oxygen vacancy concentration is then mapped through lattice expansion measurement using scanning nano-beam diffraction or 4D STEM at a spatial resolution better than 2 nm ; this allows direct determination of local oxygen vacancy diffusion coefficients in a very small domain inside pure and Sm-doped ceria at different temperatures. Further, the activation energies for oxygen transport are determined to be 0.59 , 0.66 , 1.12 , and 1.27 eV for pure CeO_2 , $\text{Ce}_{0.94}\text{Sm}_{0.06}\text{O}_{1.97}$, $\text{Ce}_{0.89}\text{Sm}_{0.11}\text{O}_{1.945}$, and $\text{Ce}_{0.8}\text{Sm}_{0.2}\text{O}_{1.9}$, respectively, implying that activation energy increases due to impurity scattering. The results are qualitatively supported by density functional theory (DFT) calculations. In addition, our *in situ* TEM investigation reveals that dislocations impede oxygen vacancy diffusion by absorbing oxygen vacancies from the surrounding areas and pinning them locally. With more oxygen vacancies absorbed, dislocations show extended strain fields with local tensile zone sandwiched between the compressed ones. Therefore, dislocation density should be reduced in order to minimize the resistance to oxygen vacancy diffusion at low temperatures.

Introduction

Pure and doped ceria (CeO_2) are widely used in systems for chemical and energy transformation processes, including fuel cells, electrolyzers, and catalytic converters for automotive applications [1,2]. It is well known that ceria doped with suitable aliova-

lent dopants, such as Sm, improves its ionic conductivity even at a relatively low temperature [3]. The Sm-doped ceria with a composition of $\text{Ce}_{0.8}\text{Sm}_{0.2}\text{O}_{1.9}$ is reported to have the highest ionic conductivity [4], making it an attractive electrolyte for intermediate-temperature solid oxide fuel cells (SOFC), which have potential to be the cleanest and most efficient power source [5]. Doped ceria is also used as a vital component in other devices (e.g., reactors) where oxygen is involved in the chemical or electrochemical reactions. In these applications, the rate of oxygen

* Corresponding authors.

E-mail addresses: Ding, Y. (yong.ding@mse.gatech.edu), Liu, M. (meilin.liu@mse.gatech.edu), Wang, Z.L. (zhong.wang@mse.gatech.edu).

† These authors contributed equally.

vacancy formation and migration in ceria is vital to its performance [6]. But owing to the disordered distribution, large spatial variation and small atomic number of oxygen, which prevent the application of X-ray diffraction and electron imaging techniques, quantitative analysis of point vacancies remains challenging in general.

Since diffusion of oxygen vacancy is a thermally activated process, the temperature dependence of oxygen vacancy diffusivity can be expressed by an Arrhenius relationship:

$$D(T) = D_0 \cdot e^{\left(-\frac{E_a}{kT}\right)} \quad (1)$$

where T stands for absolute temperature in K, k for the Boltzmann constant, D_0 for the temperature independent prefactor, and E_a for activation energy for oxygen vacancy diffusion [7,8]. Materials with a lower E_a will facilitate oxygen vacancy diffusion at low temperatures [3]. For pure CeO_2 , the activation energy (E_a) includes two components: the migration energy (E_m) of oxygen vacancy and the oxygen vacancy formation energy (E_f). On the other hand, in doped CeO_2 , the activation energy is the sum of the migration energy and association energy (E_{ass}), which is the formation energy of the dopant-vacancy associates [9–11]. As most oxygen vacancies are dissociated at high temperatures, E_{ass} could be essentially ignored. However, at low and intermediate temperatures (<600 °C), the association energy plays a key role in diffusion pathways.

Both experimental and theoretical approaches have been taken to study the diffusion of oxygen vacancies in pure and doped ceria. The major experimental techniques used to study oxygen migration in ceria include *ac* impedance analysis, gas-solid isotope exchange combined with sectioning and mass or ion beam mass spectrometry, and thin tracer layers of ^{18}O -containing oxide with sparks, laser source or secondary ion mass spectroscopy [6,12–21]. An optical *in situ* strategy was applied to measure the diffusion coefficient of an ultrathin CeO_2 layer at low temperature [22]. On the theoretical side, Andersson et al. studied dopant dependent ionic conductivity using density functional theory (DFT) calculations [3]. They revealed that the ideal dopant should have an effective atomic number between Pm and Sm. A DFT + U study has been carried out by Dholabhai et al. to show how the existence of Pr affected vacancy formation and migration in ceria [23]. Gotte et al. studied the oxygen self-diffusion in reduced CeO_2 using molecular dynamics simulation [8]. Koettgen et al. summarized numerous recent first-principles calculations and kinetic Monte Carlo (KMC) simulations on the ionic conductivity of both pure and doped ceria [24]. The results for measured and calculated activation energies for diffusion of oxygen vacancies ranged from 0.5 to 0.9 eV [24]. Some work reported the activation energies increased with dopant concentration, while others gave contrary results. Most of the theoretical works are based on bulk models, while the experimental measurements normally included grain boundary effects [21,25]. In order to understand oxygen vacancy migration in more detail, measuring oxygen vacancy diffusion inside a single crystal or a single grain is preferred.

Accurate characterization of oxygen vacancy diffusion in metal oxides requires the state-of-the-art techniques both experimentally and computationally. Although some (scan-

ning) transmission electron microscopy ((S)TEM) works could directly observe oxygen ions in oxides [26–28], quantitative characterization of oxygen vacancies is still a grand challenge. In this work, we developed a methodology to directly measure oxygen vacancy diffusion at nanoscale for the first time inside single ceria grains using *in situ* (scanning) transmission electron microscopy ((S)TEM). The increase in activation energies with increased Sm dopant concentrations have been experimentally observed at the temperature range between -20 °C to 160 °C, and the results are supported by DFT calculations. In our previous work, using *in situ* TEM, we investigated the redox processes of pure and Sm-doped CeO_2 ceramics stimulated by high-energy electron beam irradiation [29]. The reduced structure with oxygen vacancies ordering was identified as the C-type $\text{CeO}_{1.68}$ phase [30]. To take things a step further, we purposely transformed a small region ~ 30 nm in diameter inside a single grain to the $\text{CeO}_{1.68}$ phase. The concentration gradient of oxygen vacancies from the $\text{CeO}_{1.68}$ phase to the surrounding CeO_2 phase will cause the oxygen vacancies to diffuse out from the high concentration area. It makes this grain an ideal model to investigate the oxygen diffusion. Recently developed scanning nano-beam diffraction or the so-called 4-dimensional Scanning transmission electron microscopy (4D STEM) was used to measure the local strain field and the oxygen vacancy concentration distribution [31–33], as lattice expansion at different degrees of reduction has been well documented [1,34–37]. After measuring the diffusion coefficients of CeO_2 and $\text{Ce}_{1-x}\text{Sm}_x\text{O}_{2-\delta}$ at temperatures ranging from -20 °C to 160 °C, we retrieved their activation energies E_a using a standard Arrhenius relation in Eq (1).

Elastic strain can be used to manipulate the performance of metal oxide-based electrochemical devices, such as SOFCs, by accelerating their ionic conduction [38,39]. It is believed that the oxygen vacancy diffusion coefficient can be substantially increased by tensile strain and decreased by compressive strain [40]. The formation of dislocations in CeO_2 will change the strain distribution inside grains. Sun et al. studied how dislocations alter the formation, distribution and mobility of oxygen vacancies in pure and doped CeO_2 [41]. The associative interactions among the point defects in the enrichment zone and the lack of oxygen vacancies in the depletion zone slow down oxygen ion transport. However, no experimental observation has been reported to verify their theoretical predictions.

Our TEM measurements successfully reveal high-density dislocations in both pure and Sm-doped ceria grains. The pining effect of dislocations on oxygen vacancies was observed via *in situ* TEM investigation. After absorbing oxygen vacancies from its surroundings, the dislocation exhibited extended tensile and compression zones, corresponding to local oxygen vacancy enrichment and depletion. By aggregating oxygen vacancies around dislocations, the amount of mobile oxygen vacancies decreases. At the same time, the association energy is dramatically increased. As a result, the diffusion process of oxygen vacancies will be slowed down by dislocations. In order to accelerate the oxygen vacancy diffusion in the ceria electrolyte for improved SOFC performance at low temperatures, we need to reduce the number of dislocations.

Materials and methods

Experiments

$\text{Ce}_{1-x}\text{Sm}_x\text{O}_{2-\delta}$ powder (FuelCell Materials, US) and CeO_2 powder (Alfa Aesar, US) were ball-milled with ethanol for 24 hours and dried at 80 °C for 4 h. $\text{Ce}_{1-x}\text{Sm}_x\text{O}_{2-\delta}$ and CeO_2 pellets were prepared by uniaxially pressing those powders at 250 MPa and sintered at 1450 °C for 5 hours to achieve a relative density of ~98% [29]. Then the pellets were prepared for TEM investigation by mechanical thinning, following by Ar⁺ milling at 4.5 kV using a Gatan PIPS. An FEI Tecnai F30 super-twin field-emission-gun transmission electron microscope operated at 300 kV was used to acquire the TEM images, electron diffraction patterns, and 4D STEM images. A Gatan OneView camera was used to record the images and videos with exposure times as short as 0.01 second. A Gatan Tridiem 863 UHS GIF system was used to acquire the electron energy-loss spectroscopy (EELS) spectra. Gatan Model 652.MA Double-Tilt Heating Holder was used to heat the samples, while the specimen temperature is monitored by a thermocouple welded directly to the furnace body. Gatan Model 636.MA Double-Tilt Cooling Holder was used to cool the sample by liquid nitrogen. And the temperature was monitored by a calibrated silicon diode which provides a sensitive, linear temperature response. We waited for more than 10 min at each settled temperature, in order to get an even temperature and acceptable sample drifting condition.

Computational method

Spin-polarized density functional theory (DFT) calculations were executed by means of Vienna ab initio simulation package (VASP) [53,54] with the Perdew–Burke–Ernzerhof (PBE) [55] exchange–correlation functional. Ce, Sm, and O atoms were described by 12 (5s25p64f15d16s2), 11 (5s25p65d16s2), and 6 (2s2p4) valence electrons, respectively. To accurately describe the strongly correlated Ce 4f electrons, the GGA–PBE + U method was applied with an effective U value of 5.0 eV on cerium (Ce) ions similar to previous studies [9,24,47,56,57], while samarium (Sm) ions were not treated by the GGA–PBE + U because Sm ions are already localized. All GGA–PBE + U calculations were performed with a kinetic energy cut-off of 415 eV, while Monkhorst–Pack meshes with (3 × 3 × 3) k-point were used with the projector augmented wave (PAW) method [58] and Gaussian smearing of 0.20 eV. In this study, to support the experimental findings of the activation energies of oxygen vacancy diffusion, we calculated the migration energy on the basis of the previous studies [3,9,46]. The climbing image nudged elastic band (CI-NEB) method [59] was also applied to accurately locate a transition state of oxygen vacancy diffusion of bulk CeO_2 after generating of an oxygen vacancy.

Results and discussion

From our previous work [29], a high-energy converged electron beam can reduce CeO_2 grains to C-type $\text{CeO}_{1.68}$ phase due to the ionization or radiolysis effect [42]. The electron energy-loss spectroscopy (EELS) spectra in Fig. S1a reveals the Ce^{3+} ions increased after strong electron beam ($2.87 \times 10^3 \text{ A/m}^2$ or $180 \text{ e}^-/\text{\AA}^2$) irradiation. After we switched to a smaller condense lens aperture (from 100 μm to 10 μm) and spot size from 3 to 7, a cur-

rent of only 1.89 A/m^2 was obtained, causing the reduction effect to be minimized, which can be seen in the EELS spectra in Fig. S1b. Each spectrum was acquired in 5 s intervals. We did not observe clear ratio changes between the M_4 and M_5 peaks of Ce, which can be used to determine the valence of cerium ions [43].

Fig. 1a gives a schematic illustration of the 4D STEM geometry we used. A focused nanobeam with a convergent angle of 0.7 mrad rastered over the sample area. Each pixel in received 4D STEM image is a partial sum-up of an individual 2 dimensional electron diffraction pattern. Using OneView camera to scan an area in 100×100 pixel resolution, we need 200 s. The shifting of the diffraction spots relative to the center one contains the local lattice expansion information. Fig. 1b is a 4D STEM image of a high oxygen vacancies region at the center of a CeO_2 grain. The bending contour indicates the local strain field coming from chemical expansion at the high oxygen vacancy area. Fig. 1b contains 100×100 pixels. As an example, the two diffraction patterns in Fig. 1c and 1d, correspond to pixels C and D in Fig. 1b, respectively. Fig. 1c can be indexed as the [0 0 1] zone-axis of fluorite CeO_2 , while the pattern in Fig. 1d contains some extra diffraction spots and can be indexed as the [0 0 1] zone-axis of the C-type $\text{CeO}_{1.68}$. By using a virtual aperture to select the 1 1 0 diffraction spot in Fig. 1d, we get the dark-field image in Fig. 1e to show the area containing the C-type $\text{CeO}_{1.68}$ structure [44]. Fig. 1f–i give the strain field components of E_{uu} , E_{vv} , E_{uv} and Theta (See Supplementary Information), respectively. Based on the strain measurements in Fig. 1f–i, we can calculate the local lattice expansion as displayed in Fig. 1j (See Supplementary Information for the detailed expansion calculation) [45]. Compared to the dark-field image in Fig. 1e, we can see the lattice expansion gradient outside the $\text{CeO}_{1.68}$ region. The chemical expansion ε can be written as

$$\varepsilon = 0.048 \times \delta \quad (2)$$

where δ is the concentration of oxygen vacancies in $\text{CeO}_{2-\delta}$ [34].

Fig. 1k is the calculated local oxygen vacancy distribution from the lattice expansion map in Fig. 1j using Eq. (2). We recorded 4D STEM images from the same area at different times and calculated the oxygen vacancy distribution, which are displayed in Fig. 1l–o. The zero second is defined as the ending time of converged electron beam irradiation. Fig. S2 gives the dark-field images using a virtual aperture to show the area containing the $\text{CeO}_{1.68}$ phase, which shrank with elapsing time. It indicates that oxygen vacancies diffused out of the center area as well. The local maximum oxygen vacancy concentration changes with time is plotted in Fig. 1p. We plotted the maximum of oxygen vacancy concentration versus inverse time in red in Fig. 1p as well. The linear relationship fitting of the δ vs t^{-1} in Fig. 1p gives us the slope as $245 \pm 7 \text{ s}$.

Considering that the grain has a lamellar shape and limited thickness along the incident electron-beam direction, the generated oxygen vacancies are restricted to diffuse in a two-dimensional plane perpendicular to the beam direction. The typical sample thickness is between 45 nm and 70 nm as revealed by the zero-loss EELS spectra. Therefore, we can use the two-dimensional solution of the diffusion equation to explain the

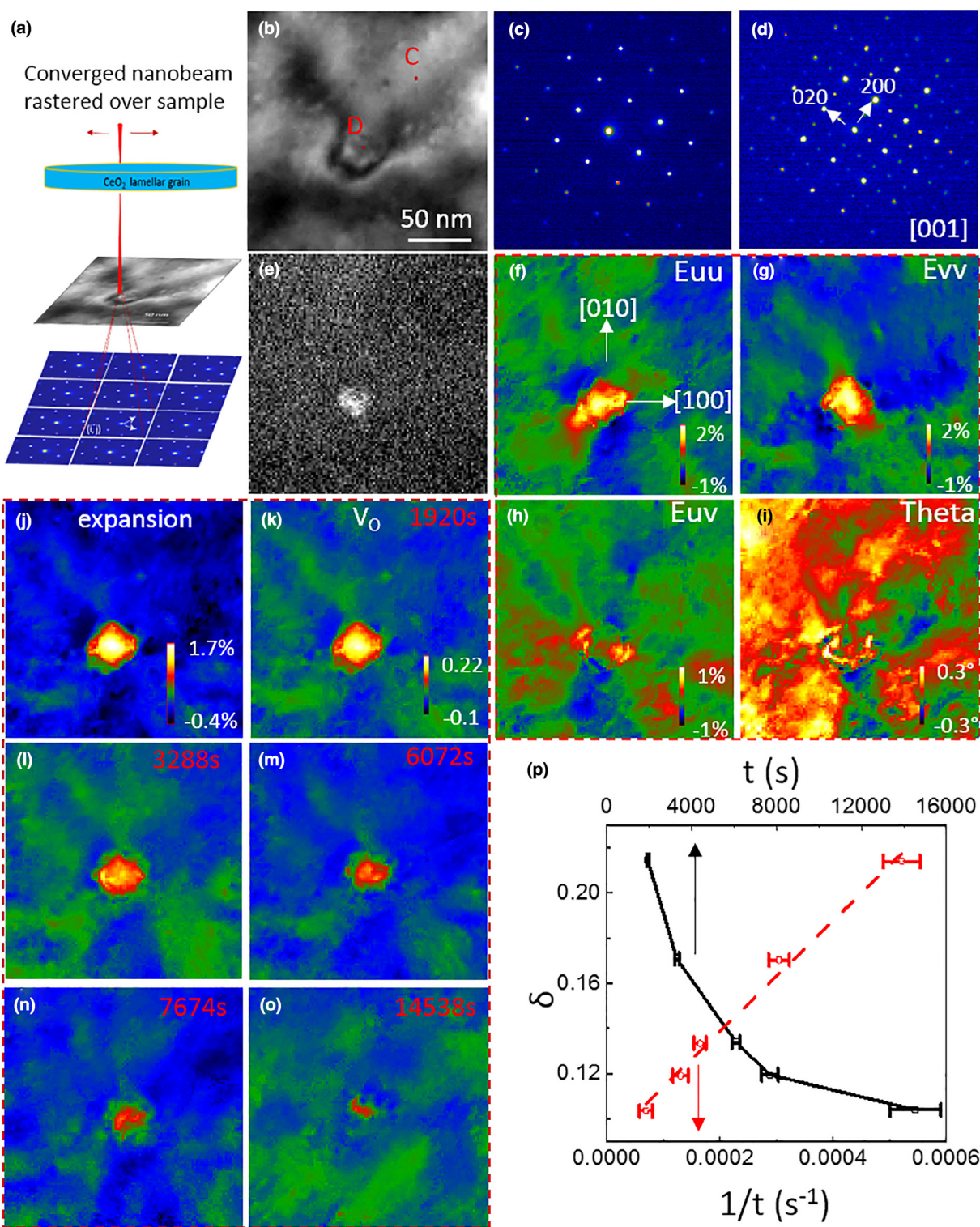


FIGURE 1

Oxygen vacancy concentration changes with time inside a CeO₂ grain. (a) Schematic illustration of the 4D STEM geometry. (b) A 4D STEM image of the whole CeO₂ grain. (c) and (d) Diffraction patterns corresponding to the two pixel points C and D in (a). (e) Dark-field image using the 1 1 0 diffraction spot in (d). (f)–(i) The strain field components calculated from (b). (j) Lattice expansion calculated from (f)–(i). (k) Oxygen vacancies distribution calculated from (j). (l)–(o) The oxygen vacancy distributions at different times. (p) Plot of maximum oxygen vacancy concentration versus time (black) and inverse time (red).

phenomenon observed in Fig. 1. The two-dimensional solution can be written as [46]

$$C(x, y, t) = \frac{M}{4\pi\sqrt{D_x D_y t}} e^{\left(-\frac{x^2}{4D_x t} - \frac{y^2}{4D_y t}\right)} \quad (3)$$

where the D_x and D_y are the diffusion coefficients along the x and y directions in the plane perpendicular to the incident electron beam. In our case, we use δ to measure the oxygen vacancy concentration as:

$$C(x, y, t) = \frac{4\delta(x, y, t)}{a^3} \quad (4)$$

where a is the lattice parameter of the fluorite unit cell. Then we have $M = \frac{4\delta_0}{a}$. Eq. (3) can be rewritten as

$$\delta(x, y, t) = \frac{\delta_0 a^2}{4\pi\sqrt{D_x D_y t}} e^{-\left(\frac{x^2}{4D_x t} + \frac{y^2}{4D_y t}\right)} \quad (5)$$

If we take an approximation of $D_x = D_y = D$ and the maximum concentration locates at the origin (0, 0), then we have

$$\delta_{max}(t) = \frac{\delta_0 a^2}{4\pi D t} \quad (6)$$

Based on the fitted slope in Fig. 1p, we calculated the diffusion coefficient of pure CeO₂ at 21.5 °C (the TEM chamber temperature) as 3.0×10^{-19} cm²/s with a 3% error.

We performed the same diffusion experiments by heating the sample inside TEM chamber to different temperatures. Fig. 2a–e show the case at temperature of 50 °C. It took 1177 s for the oxygen vacancies to diffuse out from the converged electron beam irradiated region. As shown in Eq. (6), to reach the same maximum oxygen vacancy concentration, the shorter the time

needed, the larger the diffusion coefficient will be. Therefore, the diffusion coefficient of CeO₂ at 50 °C is 3.7×10^{-18} cm²/s.

Fig. 2f–i show the case at 100 °C. We cannot acquire 4D STEM images as the diffusion process was too fast. It takes 200 s to record a 100×100 pixel 4D STEM image using our microscope, and it only took 89 s for all the generated oxygen vacancies to fully diffuse out to the surroundings as revealed by the bright-field TEM images in Fig. 2f–i. As we know the local strain field will cause strain contrast in TEM images, tracking the changes in diffraction contrast can serve the same purpose recording the diffusion time. The diffusion coefficient could be calculated as 4.9×10^{-17} cm²/s. Increasing the temperature to 160 °C, shortened the diffusion time to 8 seconds (Video S1) and the diffusion coefficient increased to 5.5×10^{-16} cm²/s. When the temperature was increased to 200 °C and higher, diffusion became so fast that we could not track the diffusion process anymore (Fig. S3a).

We recorded the EELS spectra from the same area of a CeO₂ grain at different temperatures as shown in Fig. S1c. There is no evidence of a change in ratio between the M₄ and M₅ peaks of Ce ions while we increased the temperature. Therefore, we can assume that the changes in diffusion coefficients in the range from 21.5 °C to 160 °C is mostly temperature dependent inside a pure CeO₂ grain.

With Sm doped into CeO₂ grains, the oxygen vacancy diffusion speed increased dramatically compared to pure CeO₂ at the same temperature. The diffusion scenario at a temperature

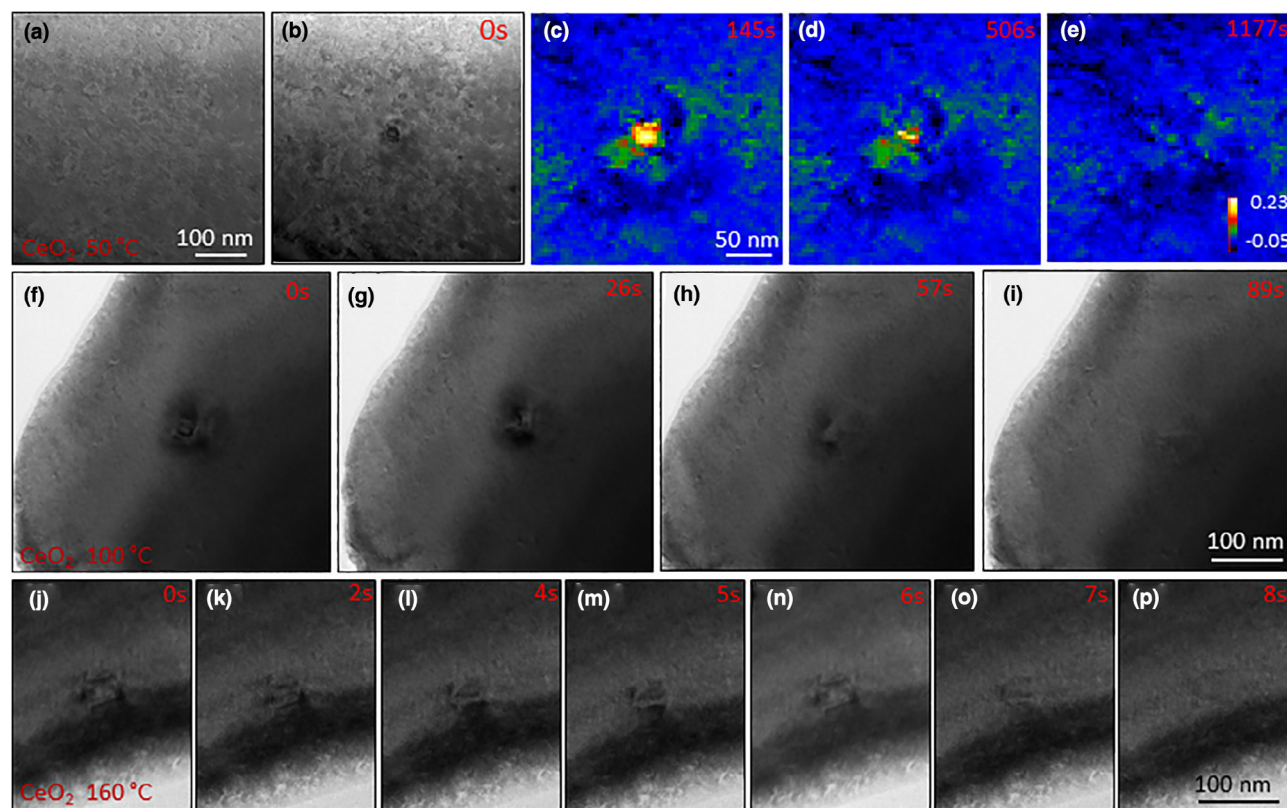


FIGURE 2

Oxygen vacancy diffusion in a CeO₂ grain with increasing temperature. (a)–(e) The diffusion process observed at 50 °C. (f)–(i) The diffusion process observed at 100 °C. (j)–(p) The diffusion process observed at 160 °C.

of 25 °C in a $\text{Ce}_{0.94}\text{Sm}_{0.06}\text{O}_{1.97}$ grain is displayed in Figs. 3a–e. The composition was measured using the EELS spectrum in Fig. S4a. The strain contrast due to the high oxygen vacancy concentration vanished in only 4 seconds (Video S2). The corresponding diffusion coefficient is $1.1 \times 10^{-15} \text{ cm}^2/\text{s}$, almost three orders of magnitude higher than that of pure CeO_2 . Increasing temperature will accelerate oxygen vacancy diffusion. Therefore, we cooled the sample down to measure the diffusion coefficients at low temperatures. Fig. 3f–j show that the diffusion process took 41 seconds at 0 °C inside the same grain as displayed in Fig. 3a–e, while Fig. 3k–o show that the time increased to 370 s at –20 °C. The calculated diffusion coefficients of $\text{Ce}_{0.94}\text{Sm}_{0.06}\text{O}_{1.97}$ at 0 °C and –20 °C are $1.1 \times 10^{-16} \text{ cm}^2/\text{s}$ and $1.2 \times 10^{-17} \text{ cm}^2/\text{s}$, respectively.

We measured the diffusion processes of $\text{Ce}_{0.89}\text{Sm}_{0.11}\text{O}_{1.945}$ and $\text{Ce}_{0.8}\text{Sm}_{0.2}\text{O}_{1.9}$ grains as well, which are displayed in Figs. S5 and S6 and videos S3 and S4. At 21.5 °C, the diffusion of oxygen vacancies was so fast that we could not even observe strain contrast after converged electron beam irradiation (Figs. S3b and S3c). However, the formation of C-type $\text{CeO}_{1.68}$ has been confirmed by high-resolution transmission electron microscopy (HRTEM) images as displayed in Fig. S7, in which the long-range lattice ordering can be clearly observed. After we expanded the electron beam to lower the beam density, we lost long-range ordering. With a converged electron beam, the ordered structure reappeared. The calculated diffusion coefficients are plotted in Fig. 4a together with those from CeO_2 and $\text{Ce}_{0.94}\text{Sm}_{0.06}\text{O}_{1.97}$ grains.

We measured the oxygen vacancy diffusion in grains of ceria with higher Sm doping, such as $\text{Ce}_{0.7}\text{Sm}_{0.3}\text{O}_{1.85}$. However, we cannot track the strain field caused by converged electron beam irradiation even at temperatures as low as of –50 °C. It may be due to the weak strain field caused by the relatively small lattice expansion. The oxygen vacancy concentration in the $\text{Ce}_{0.7}\text{Sm}_{0.3}\text{O}_{1.85}$ grain is much closer to the C-type $\text{Ce}_2\text{O}_{1.68}$ phase compared to cases in grains with lower Sm concentrations as shown in Figs. 1–3 and Figs. S5 and S6.

After calculating the diffusion coefficients at different temperatures, the activation energy E_a for oxygen vacancy migration was retrieved using a standard Arrhenius relation, shown in Eq. (1). Fig. 4a gives these Arrhenius plots of the diffusion coefficients from the grains with different Sm concentrations. For pure CeO_2 , the E_a is $0.59 \pm 0.01 \text{ eV}$ (or $56.6 \pm 1.25 \text{ kJ/mol}$) and the D_0 is $4.0 \times 10^{-9} \text{ cm}^2/\text{s}$. It is very close to the calculated results [8,24]. While for $\text{Ce}_{0.94}\text{Sm}_{0.06}\text{O}_{1.97}$, $\text{Ce}_{0.89}\text{Sm}_{0.11}\text{O}_{1.945}$ and $\text{Ce}_{0.8}\text{Sm}_{0.2}\text{O}_{1.9}$, the E_a increased to 0.66 eV, 1.12 eV and then 1.27 eV, respectively. The corresponding D_0 are $1.7 \times 10^{-4} \text{ cm}^2/\text{s}$, $2.2 \times 10^5 \text{ cm}^2/\text{s}$ and $2.8 \times 10^8 \text{ cm}^2/\text{s}$, respectively. Higher dopant concentration means more scattering from dopants to oxygen vacancies in their diffusion pathway. With more Sm doped into CeO_2 grains, both the temperature independent prefactor D_0 and activation energy E_a increased, while the prefactor D_0 increases much more dramatically. The high activation energy will impede oxygen vacancy diffusion. However, combined with the high D_0 , the doped ceria still show improved oxygen vacancy diffusion coefficient.

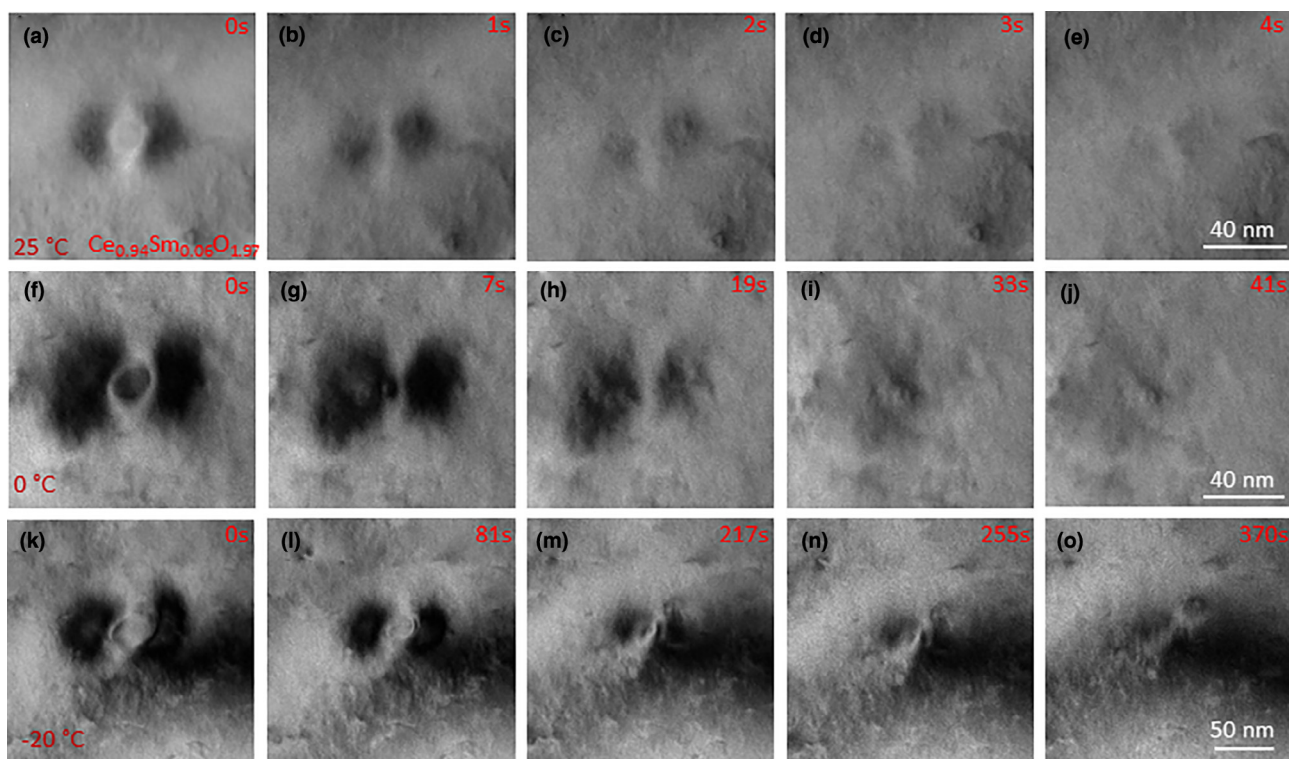


FIGURE 3

Oxygen vacancy diffusion in a $\text{Ce}_{0.94}\text{Sm}_{0.06}\text{O}_{1.97}$ grain. (a)–(e) The diffusion process observed at 25 °C. (f)–(j) The diffusion process at 0 °C. (k)–(o) The diffusion process at –20 °C.

The plots in Fig. 4b show the retrieved and measured diffusion coefficients at 0 °C and their activation energies correspond to different doping concentrations of Sm. We can see the dramatic increase in diffusion coefficients at the low doping concentration (from 0% to 6%). With more Sm doped inside the grain, the diffusion coefficients close to saturated at 20% concentration. It was reported that the increase of the oxygen vacancy concentration could decrease the migration energy (E_m) of oxygen vacancy diffusion [24], while high density of oxygen vacancies would enhance the interactions between the dopants and oxygen vacancies as well [10]. Therefore, the association energy (E_{ass}) may be increased dramatically by Sm doping in CeO_2 . As our measurements were performed at low temperatures (−20 °C to

160 °C), our measured activation energies of oxygen vacancy diffusion can be explained as the combination of the migration and association energies ($E_a = E_m + E_{ass}$) [3]. The maximum ionic conductivity at 20% Sm doping could be considered as the balance between the increased D_0 and activation energy at low and intermediate temperatures. The increase of our measured activation energies with Sm doping is consistent with those measured using an AC impedance method at the temperature range of 240–1000 °C [21].

To understand the increase of the activation energies of oxygen vacancy diffusion as Sm is doped in CeO_2 , we performed DFT + U calculations with an effective U value of 5.0 eV. Our previous studies [47,48] on stoichiometric and oxygen deficient

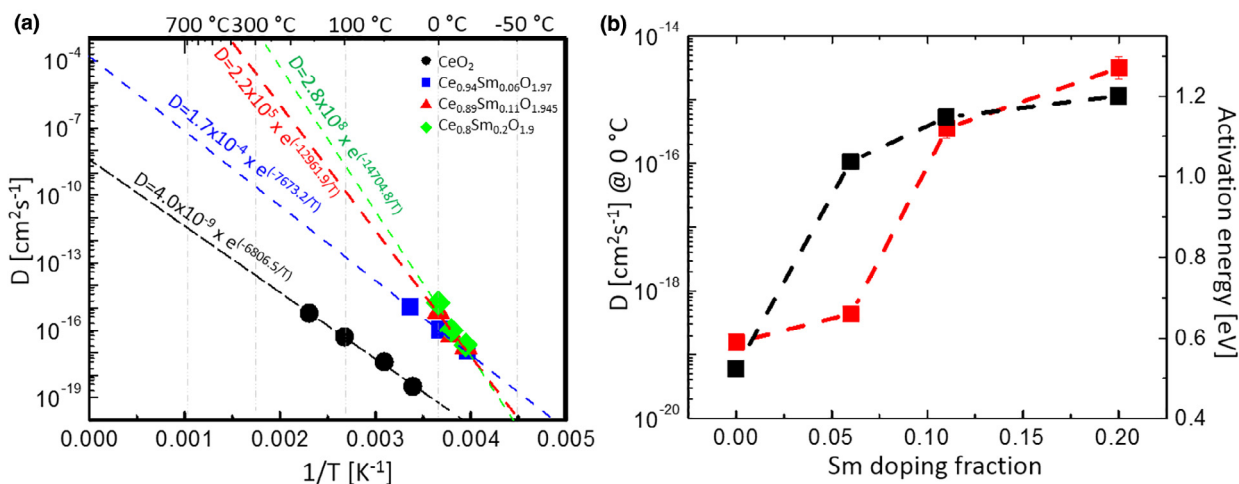


FIGURE 4

Activation energy retrieved from a standard Arrhenius relation. (a) Arrhenius plots of oxygen vacancies diffusion coefficients in the temperature range of −20 to 160 °C. (b) The change in diffusion coefficients and activation energies with different Sm doping concentrations.

TABLE 1

Summary of oxygen vacancy diffusion in pure and Sm-doped ceria. Exp., MD and DFT stand for experimental measurement, molecular dynamics, and density functional theory, respectively.

Sample	D_0 cm^2/s	E_a eV	Temperature K	Ref.
CeO_2	4×10^{-9}	0.59	253–433	Exp.; this work
$Ce_{0.94}Sm_{0.06}O_{1.97}$	1.7×10^{-4}	0.66	253–433	Exp.; this work
$Ce_{0.89}Sm_{0.11}O_{1.945}$	2.2×10^5	1.12	253–433	Exp.; this work
$Ce_{0.8}Sm_{0.2}O_{1.9}$	2.8×10^8	1.27	253–433	Exp.; this work
CeO_2		0.42		DFT; this work
$Ce_{0.937}Sm_{0.063}O_{1.98}$		1.15		DFT; this work
$Ce_{0.969}Sm_{0.031}O_{1.99}$		1.18		DFT; this work
$CeO_{1.8778}$	5.7×10^{-5}	0.55	800–2200	MD; ref. [8]
$CeO_{1.92}$	1.5×10^{-5}	0.51	1123–1423	Exp.; ref. [3]
$Ce_{0.9}Sm_{0.1}O_{1.95}$		0.49	>495	Exp.; ref. [21]
		0.72	<495	
$Ce_{0.8}Sm_{0.2}O_{1.9}$		0.61	>492	Exp.; ref. [21]
		0.89	<492	
CeO_2	2.55×10^{-16}	0.28	323–473	Exp.; ref. [22]
$Ce_{0.934}Sm_{0.066}O_{1.967}$		0.43		DFT; ref. [9]
		0.73		
$Ce_{0.958}Sm_{0.042}O_{1.979}$		0.66		DFT; ref. [3]
$Ce_{0.937}Sm_{0.063}O_{1.98}$		1.12	300	DFT; ref. [52]
		1.19	700	
		1.28	1000	

CeO₂ systems clearly manifested that the 4f electrons are fully localized on two cerium ions near an oxygen vacancy, including its computed band gaps. As an initiative, to construct realistic bulk models, we accurately located a transition state by using the CI-NEB method with the (Ce₃₂O₆₃)²⁺ model (Fig. S8), where the superscript refers to its charge. It clearly shows that its diffusion occurs on the diffusion axis as reported [24,49] (Fig. S9) and its migration barrier locates at the midpoint between two cerium ions [3,9,24,49] with the migration energy (E_m) of 0.34 eV. Similar to the previous studies [3,9,24,49], to save the computational time, we calculated the migration energy of oxygen vacancy diffusion by placing an oxygen ion at the midpoint of two cerium ions (Fig. S10a), leading to 0.42 eV, which is in good agreement with our CI-NEB result. Therefore, we assumed that this approach for estimating a migration energy of oxygen vacancy diffusion may be valid to apply for more realistic bulk models, such as (4 × 2 × 2) supercell models (3.1% Sm-doped CeO₂;

Fig. S11). We, then, calculated a migration energy of oxygen vacancy diffusion using the (Ce₆₄O₁₂₇)²⁺ model after generating one oxygen vacancy (~0.8%), leading to that of 0.43 eV. Our calculated migration energy of 0.42 and 0.43 eV using pure CeO₂ models are in excellent agreement with the computed [23] and experimental [50,51] results of 0.47 eV and 0.49–0.76 eV, respectively. In particular, it is in line with our measured activation energy of pure CeO₂ of 0.59 eV using *in situ* TEM. Then to explore the oxygen vacancy diffusion in Sm-doped CeO₂, we prepared (Ce₃₂Sm₂O₆₃)⁰ and (Ce₆₂Sm₂O₁₂₇)⁰ (Figs. S8 and S11). The previous studies [24,49] proposed the Ce-(TS)-Sm and Sm-(TS)-Sm edge configurations for estimating the migration energy of oxygen vacancy diffusion in the Sm-doped CeO₂ system, where TS stands for transition state. However, in this study, we only considered the Sm-(TS)-Sm configuration as the extreme (Fig. S10b). As summarized in Table S1, it results in the migration energies of 1.15 and 1.18 eV, respectively, using (Ce₃₂Sm₂O₆₃)⁰

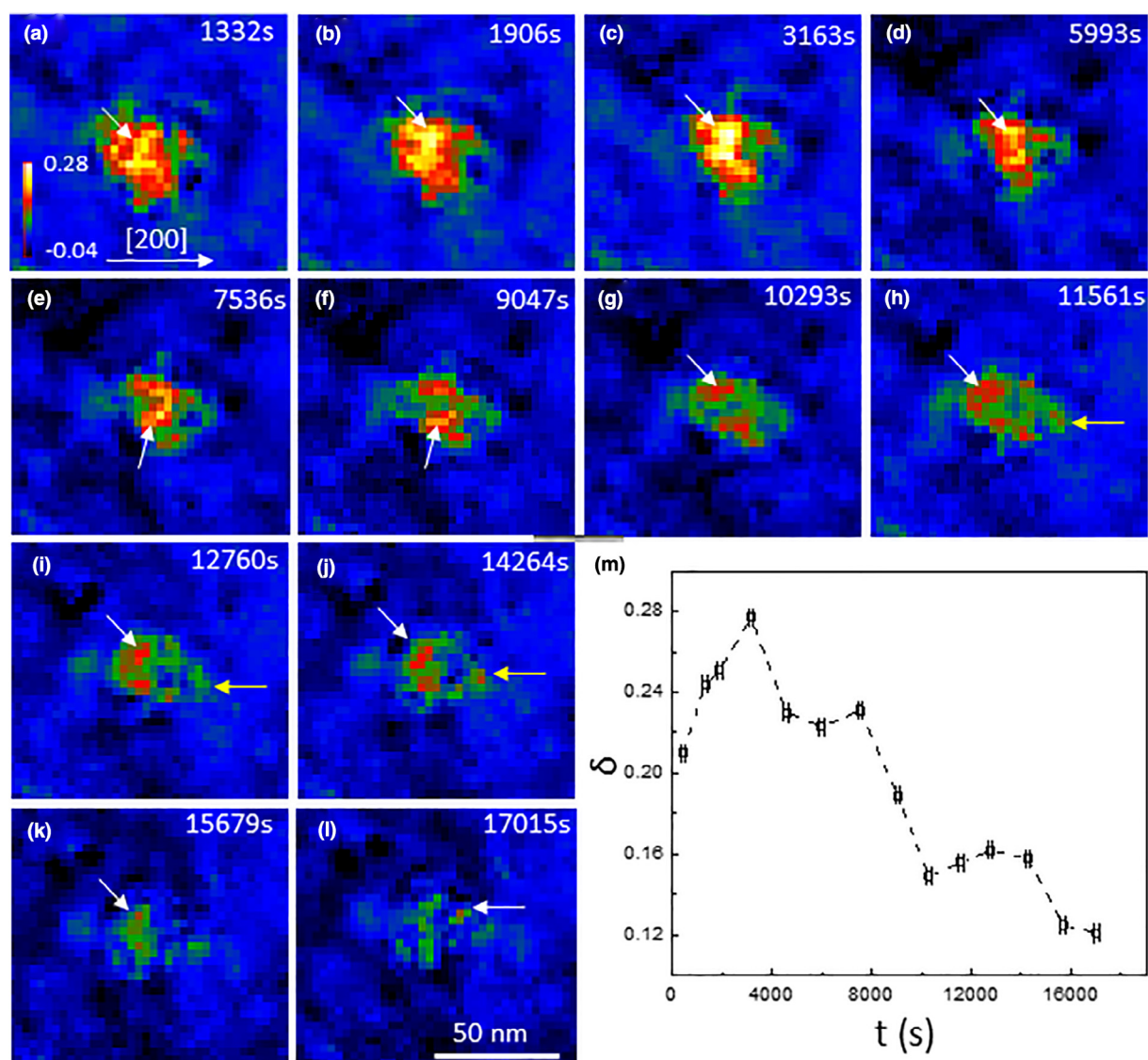


FIGURE 5

Abnormal oxygen vacancy concentration increases at dislocation sites. (a)–(l) Oxygen vacancy concentration distributions at different times. The maximum concentration point shifted with time from one dislocation site to another. (m) Plot of maximum oxygen vacancy concentration with respect to time.

and $(\text{Ce}_{62}\text{Sm}_{2}\text{O}_{127})^0$, which are in good agreement with the previous computed migration energy [52]. Since all of possible configurations could not be considered by means of DFT calculations, in this study, we computationally verified that as pure ceria is doped by Sm ions, it requires higher activation energies. As discussed above [49], its association energy is highly contributed to the activation energy of oxygen vacancy diffusion. In addition, a small doping can cause strong dopant-oxygen vacancy associates, leading to thermodynamically a significant increase of migration entropy [52]. The experimental and computed results of the activation energies of pure and Sm doped ceria are compiled in Table 1. Our measured results have a good match with most of the reported data. The comparable low activation energy of 0.28 eV in Ref. [22] may be caused by the ultra-thin sample, which is a 2–10 nm thick CeO_2 film.

Our measured activation energies of oxygen vacancy diffusion for pure ceria is larger than the simulated ones. It cannot be the grain boundary effect [21,24], for our measurements were carried out inside a single ceria grain. Highly possibly, it is due to the

pinning effect of dislocations. There is a high density of dislocations in pure and doped CeO_2 grains [29]. Fig. S12 gives the low and high magnification TEM images of a CeO_2 grain. The counted dislocation density can reach $1.2 \times 10^8 \text{ cm}^{-2}$. If the initial converged electron beam irradiated region contained some dislocations, the diffusion process may be elongated as shown in Fig. 5, in which the oxygen vacancies mapping calculated from the 4D STEM images is recorded over time. The trend of δ changed with time and the inverse of time are plotted separately in Fig. 5m and S13, respectively. Unlike the case in Fig. 1, the maximum δ did not continuously decrease with time. Three periods with an unusual increase in δ can be identified in Fig. 5m. We marked the maximum δ point in each mapping with a white arrowhead in Fig. 5a–l. Actually, these maximum δ points did not all correspond to the same site. Comparing the oxygen vacancies mappings with the TEM bright-field images in Figs. S14a, S14b and S14c, which were recorded before and after converged electron beam to do the irradiation, we can trace the δ maximum points to the two dislocations in the left side of the

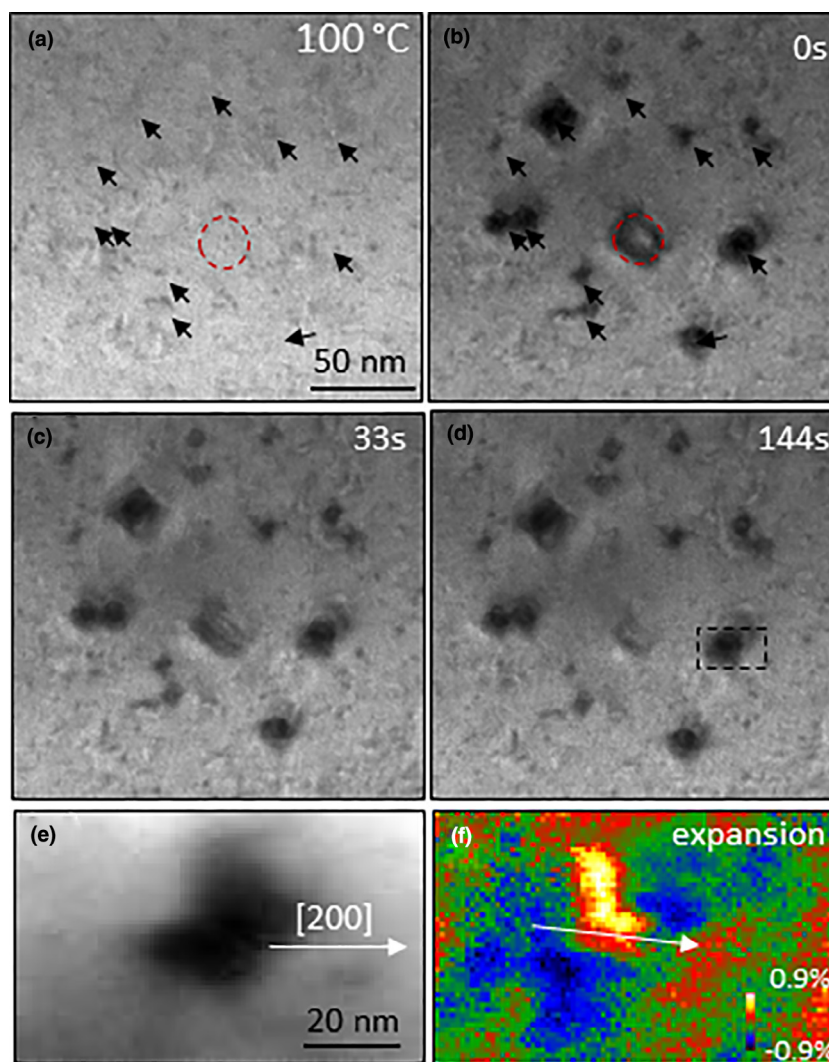


FIGURE 6

The oxygen vacancies absorption effect of dislocations observed at 100 °C in a CeO_2 grain. (a) Before converged electron beam irradiation, dislocations show weak contrast. (b)–(d) TEM images recorded in time sequence after the irradiation. Dislocations show extended contrast. (e) 4D STEM image from the black dashed rectangle marked area in (d). (f) Lattice expansion mapping from the same area in (e).

irradiated region, which are marked by white arrowheads in Fig. S14b. From 1332 s to 5993 s, the maximum δ was located at the top left dislocation, while from 5993 s to 9047 s, the maximum δ was located at the bottom left dislocation. From 10293 s to 15679 s, the maximum δ shifted back to the top left dislocation again. We also noticed from 10293 s to 14264 s, the local oxygen vacancy concentration at the right dislocation (marked by yellow arrowhead) increased, although they are not the maximum point in the mapping. The unusual increase in the oxygen vacancy concentration at the dislocation sites reveals the absorption effect of dislocations on the oxygen vacancies. The oxygen vacancies diffuse ten times slower at the dislocation sites than that at perfect grain site as revealed from the relationship between δ and the inverse of time in Fig. S13. It is reasonable that the dislocation absorbed the oxygen vacancies and pinning them locally, and then slowed down the oxygen vacancies in further diffusion. This can be clearly seen in Fig. 5, which shows much longer diffusion process than the case as mentioned in Fig. 1.

With increasing oxygen vacancy diffusion coefficients with temperature, the pinning effect of dislocations on oxygen vacancies will become more obvious. Fig. 6 gives a series of images to show the diffusion process inside a CeO₂ grain at 100 °C. Before the electron beam was purposely focused to generate high oxygen vacancies region in the center, a bright-field TEM image in Fig. 6a gives very weak contrast of the dislocations, which are marked with arrowheads. After strong electron beam irradiation, we can see the high concentration of oxygen vacancies caused strain contrast at the center. At the same time, the dislocations surrounding the high oxygen vacancy region show enhanced and extended contrast, which means a stronger strain field around them. Such contrast from the dislocations was stable even after the center high oxygen vacancies region lost its strain contrast in Fig. 6d. The normal strain field around a dislocation only spans around 2 nm from the core as displayed in Fig. S15. However, the strain field of dislocations in Fig. 6 covered an area over 20 nm in size. We recorded a 4D STEM image in Fig. 6e from the marked dislocation in Fig. 6d. The calculated lattice expansion around the dislocation is depicted in Fig. 6f. While the local strain and oxygen vacancies mappings are displayed in Fig. S16. We can see that the lattice expansion zone is sandwiched by two compressed ones. The white arrowhead in Fig. 6f highlights the oxygen vacancy diffusion direction away from the center high concentration region. The compressed area (in blue color) corresponds to the oxygen vacancy depletion zone, which would dramatically slow down oxygen vacancy diffusion. Only 89 s is needed for the high oxygen vacancies area to diffuse out completely in Fig. 2f-2i. However, in the diffusion process in Fig. 6, we can still observe strain contrast from the center area after 144 s. The dislocations can absorb oxygen vacancies from their surrounding and pin them locally. As a result, the pinned oxygen vacancies lose mobility and cannot contribute to further diffusion. The extended strain field around the dislocations slowed down oxygen vacancy diffusion. Such pinning effect of dislocation on oxygen vacancies was also observed in Sm doped CeO₂. Video S2 gives one example in a Ce_{0.94}Sm_{0.06}O_{1.97} grain. The extended strain field around the dislocation is very stable, while the converged electron beam irradiation generated high oxygen vacancies region lost contrast within several seconds.

Conclusions

By using *in situ* (S)TEM investigation, we have successfully measured the oxygen vacancy diffusion coefficients for single grains of CeO₂, Ce_{0.94}Sm_{0.06}O_{1.97}, Ce_{0.89}Sm_{0.11}O_{1.945} and Ce_{0.8}Sm_{0.2}O_{1.9} at -20 °C to 160 °C and calculated their activation energies as 0.59 eV, 0.66 eV, 1.12 eV, and 1.27 eV, respectively, implying activation energy increases due to impurity scattering. A dramatic increase in the diffusion coefficients was observed at low doping concentration (from 0% to 6%), while a saturation in enhancement of diffusion coefficient is approached at around 20% doping concentration. The maximum ionic conductivity is reached at ~20% concentration of Sm doping due to a compromise between the increase in vacancy concentration and association effect (that diminishes the diffusivity). The absorption of oxygen vacancies by dislocations, or aggregation of oxygen vacancies around the dislocations, results in smaller amount of mobile oxygen vacancies and larger association energy of local defects; thus, oxygen vacancy diffusion will be slowed down by the dislocations. In order to facilitate fast diffusion of oxygen vacancy at low temperatures, it is necessary to minimize the density of dislocations in ceria grains.

Credit author statement

Y.D., M.L. and Z.W. conceived the project. Y.D. carried out the TEM work. Y. Choi executed the DFT calculations. Y. Chen fabricated the ceramic samples. Y.D. and Y. Choi co-wrote the draft. All authors contributed to discussions on the manuscript. K.P., M.L. and Z.W. revised the manuscript.

Acknowledgements

This work was supported by the Hightower Chair Foundation, the National Science Foundation (DMR-1505319), the US Department of Energy EERE Hydrogen and Fuel Cell R&D Program (DE-EE0008439), and the Higher Education Sprout Project of the National Chiao Tung University and Ministry of Education (MOE), Taiwan. DFT calculations were performed using the resources of the National Energy Research Scientific Computing Center (NERSC), a U.S. Department of Energy Office of Science User Facility operated under Contract No. DE-AC02-05CH11231. We are grateful to the National Center for High-performance Computing (NCHC) for computer time and facilities.

Appendix A. Supplementary data

Supplementary data to this article can be found online at <https://doi.org/10.1016/j.mattod.2020.04.006>.

References

- [1] A. Trovarelli, *Catalysis by Ceria and Related Materials* 12 (2013) 1–888.
- [2] M. Mogensen, N.M. Sammes, G.A. Tompsett, *Solid State Ionics* 129 (2000) 63–94.
- [3] D.A. Andersson, S.I. Simak, N.V. Skorodumova, I.A. Abrikosov, B. Johansson, *PNAS* 103 (2006) 3518–3521.
- [4] K. Eguchi, T. Setoguchi, T. Inoue, H. Arai, *Solid State Ionics* 52 (1992) 165–172.
- [5] Y. Chen, B. deGlee, Y. Tang, Z.Y. Wang, B.T. Zhao, Y.C. Wei, L. Zhang, S. Yoo, K. Pei, J.H. Kim, Y. Ding, P. Hu, F.F. Tao, M.L. Liu, *Nature, Energy* 3 (2018) 1042–1050.
- [6] O.T. Sørensen, *Nonstoichiometric Oxides*, Academic Press, New York, 1981.

- [7] D.M. Smyth, *The Defect Chemistry of Metal Oxides*, Oxford University Press, Oxford, 2000.
- [8] A. Gotte, D. Spangberg, K. Hermansson, M. Baudin, *Solid State Ionics* 178 (2007) 1421–1427.
- [9] A. Ismail, J. Hooper, J.B. Giorgi, T.K. Woo, *PCCP* 13 (2011) 6116–6124.
- [10] T. Zacherle, A. Schrieffer, R.A. De Souza, M. Martin, *Phys. Rev. B* 87 (2013) 134104.
- [11] M. Alaydrus, M. Sakaue, S.M. Aspera, T.D.K. Wungu, T.P.T. Linh, H. Kasai, T. Ishihara, T. Mohri, *J. Phys.-Condens. Matter* 25 (2013) 225401.
- [12] Y. Oishi, W.D. Kingery, *J. Chem. Phys.* 33 (1960) 480–486.
- [13] J.F. Marin, P. Contamin, *J. Nucl. Mater.* 30 (1969) 16.
- [14] R. Freer, *J. Mater. Sci.* 15 (1980) 803–824.
- [15] M. Kamiya et al., *J. Electrochem. Soc.* 147 (2000) 1222–1227.
- [16] D. Martin, D. Duprez, *J. Phys. Chem.* 100 (1996) 9429–9438.
- [17] S. Ackermann, J.R. Scheffe, A. Steinfeldt, *J. Phys. Chem. C* 118 (2014) 5216–5225.
- [18] M. Burriel et al., *Chem. Mater.* 24 (2012) 613–621.
- [19] M. Kamiya et al., *J. Mater. Res.* 16 (2001) 179–184.
- [20] M. Nauer, C. Ftikos, B.C.H. Steele, *J. Eur. Ceram. Soc.* 14 (1994) 493–499.
- [21] Z.L. Zhan, T.L. Wen, H.Y. Tu, Z.Y. Lu, *J. Electrochem. Soc.* 148 (2001) A427–A432.
- [22] P. Neuderth et al., *Adv. Energy Mater.* 8 (2018) 1802120.
- [23] P.P. Dholabhai et al., *J. Chem. Phys.* 132 (2010) 094104.
- [24] J. Koettgen et al., *PCCP* 20 (2018) 14291–14321.
- [25] D.S. Aidhy, Y.W. Zhang, W.J. Weber, *J. Mater. Chem. A* 2 (2014) 1704–1709.
- [26] C.L. Jia, M. Lentzen, K. Urban, *Science* 299 (2003) 870–873.
- [27] C.L. Jia, M. Lentzen, K. Urban, *Microsc. Microanal.* 11 (2005) 113–115.
- [28] S.D. Findlay et al., *Appl. Phys. Lett.* 95 (2009) 191913.
- [29] Y. Ding et al., *J. Appl. Phys.* 120 (2016) 214302.
- [30] E.A. Kummerle, G. Heger, *J. Solid State Chem.* 147 (1999) 485–500.
- [31] V.B. Ozdol et al., *Appl. Phys. Lett.* 106 (2015) 253107.
- [32] C. Gammer et al., *Appl. Phys. Lett.* 109 (2016) 081906.
- [33] C. Ophus et al., *Appl. Phys. Lett.* 110 (2017) 063102.
- [34] D. Marrocchelli et al., *Adv. Funct. Mater.* 22 (2012) 1958–1965.
- [35] M.J.D. Rushton, A. Chronos, *Sci. Rep.* 4 (2014) 6068.
- [36] S.R. Bishop, K.L. Duncan, E.D. Wachsman, *Electrochim. Acta* 54 (2009) 1436–1443.
- [37] S.R. Bishop et al., *J. Eur. Ceram. Soc.* 31 (2011) 2351–2356.
- [38] J. Ahn et al., *ACS Appl. Mater. Interfaces* 9 (2017) 42415–42419.
- [39] D.S. Aidhy, Y.W. Zhang, W.J. Weber, *J. Phys. Chem. C* 118 (2014) 4207–4212.
- [40] M.J.D. Rushton et al., *Solid State Ionics* 230 (2013) 37–42.
- [41] L.X. Sun, D. Marrocchelli, B. Yildiz, *Nat. Commun.* 6 (2015) 6294.
- [42] R.F. Egerton, P. Li, M. Malac, *Micron* 35 (2004) 399–409.
- [43] L.A.J. Garvie, P.R. Buseck, *J. Phys. Chem. Solids* 60 (1999) 1943–1947.
- [44] C. Gammer et al., *Ultramicroscopy* 155 (2015) 1–10.
- [45] P.A. Kelly, *Mechanics Lecture Notes: An Introduction to Solid Mechanics*.
- [46] S.A. Socolofsky, G.H. Jirka, *Special Topics in Mixing and Transport Processes in the Environment*, 5th ed., College Station, 2005.
- [47] Y. Choi et al., *PCCP* 16 (2014) 22588–22599.
- [48] H.-T. Chen et al., *ChemPhysChem* 8 (2007) 849–855.
- [49] M. Nakayama, M. Martin, *PCCP* 11 (2009) 3241–3249.
- [50] S.B. Adler, J.W. Smith, J.A. Reimer, *J. Chem. Phys.* 98 (1993) 7613–7620.
- [51] H.L. Tuller, A.S. Nowick, *J. Phys. Chem. Solids* 38 (1977) 859–867.
- [52] J. Koettgen et al., *Phys. Rev. B* 97 (2018) 024305.
- [53] G. Kresse, J. Hafner, *Phys. Rev. B* 47 (1993) 558–561.
- [54] G. Kresse, J. Furthmuller, *Phys. Rev. B* 54 (1996) 11169–11186.
- [55] J.P. Perdew, K. Burke, M. Ernzerhof, *Phys. Rev. Lett.* 77 (1996) 3865–3868.
- [56] Z. Lu, Z. Yang, *J. Phys.: Condens. Matter* 22 (2010) 475003.
- [57] M. Nolan et al., *Surf. Sci.* 576 (2005) 217–229.
- [58] P.E. Blöchl, *Phys. Rev. B* 50 (1994) 17953–17979.
- [59] G. Henkelman, B.P. Uberuaga, H. Jónsson, *J. Chem. Phys.* 113 (2000) 9901–9904.